PAPER

Check for updates

Methylation modification of coal gasification fine slag for enhanced organic dye adsorption in wastewater

Changwei Bai and Jing Yang [ID] *

The disposal of coal gasification fine slag (CGFS) and the treatment of dye wastewater present substantial environmental pressures. Therefore, developing cost-effective adsorbents is crucial. In this study, CGFS-based adsorbents, which are modified with dimethyl diethoxy silane (DDS-CGFS) and dodecyl trimethyl ammonium chloride (DTAC-CGFS), were prepared and applied for the removal of rhodamine B (RhB) organic dye. The adsorption performances were evaluated across different pH values, temperatures, and contact time. Under optimal conditions (pH = 7, 328.15 K, 24 h), the DDS-CGFS adsorbent exhibited a maximum adsorption capacity of 92.82 mg g^{-1} for rhodamine B. Kinetic and isotherm analyses revealed that the adsorption involved both physical and chemical processes. The intra-particle diffusion model suggested that the adsorption kinetics were governed by boundary-layer and intra-particle diffusions. Thermodynamic parameters ($\Delta G° < 0$, $\Delta H° > 0$, $\Delta S° > 0$) indicated that the adsorption was a spontaneous and endothermic process accompanied by an increase in entropy. Material characterization and model fitting suggested a synergistic adsorption mechanism, potentially involving interactions such as hydrogen bonding and $\pi-\pi$ stacking. Overall, DDS-CGFS and DTAC-CGFS are low-cost adsorbents for remediating dye wastewater. Due to their outstanding adsorption capacity, they show potential as ideal adsorbents for dye wastewater treatment.

1 Introduction

The widely employed coal gasification technology has contributed to unprecedented advancements in the current coal chemical industry.[1] Coal gasification fine slag (CGFS) is one of the main by-products of coal gasification process; its annual discharge has reached millions of tons in China and is constantly increasing with the promotion of clean coal technology.[2] Because of the small particle sizes (0–150 μm) of CGFS, its high ash content (about 84 wt%), and the presence of heavy metals, such as Cr, Mn, and V, the traditional storage and treatment method easily causes air pollution, land resource waste, groundwater pollution and other environmental problems.[3] At the same time, the inhalation of the accumulated coal cinder poses health risks to the human body.[4] Studies have shown that the chemical composition of CGFS is dominated by inorganic minerals, such as SiO$_2$, Al$_2$O$_3$ and CaO, and contains a large amount of residual carbon, which provides a unique advantage for its resource utilization.[5] Dye wastewater is a type of industrial wastewater, which mainly originates from printing, dyeing, and dye production processes. Organic dyes, such as rhodamine B (RhB), malachite green (MG), methyl orange (MO), methylene blue (MB), dispersed deep blue (H-GL),

and reactive brilliant orange (K-GN), can cause harm to the environment.[6-9] Dye wastewater is difficult to degrade and persists in water for a long time, posing harm to organisms and making water quality evaluation difficult.[10,11] At present, the common methods for removing dye wastewater are adsorption,[12] membrane separation,[13] electrochemical oxidation,[14] ozone oxidation,[15] *etc.* Among the many methods, adsorption is considered the most effective owing to its advantages of simple operation and high efficiency.[16] At present, the materials commonly used in adsorption are activated carbon,[17] bentonite[18] biochar,[19] covalent organic frameworks/polymers,[20] metal organic frameworks,[21] zeolites[22] *etc.* However, the use of these materials is limited by their high cost. Therefore, the development of high-performing and low-cost adsorbents using CGFS is urgently needed.

In recent years, researchers have focused on transforming CGFS into high-value-added materials for dye wastewater treatment. Treated CGFS can be used as a high-efficiency adsorbent for dye wastewater. For example, Huang *et al.*[23] converted CGFS into adsorbents with high specific surface area, large pore volume and abundant surface functional groups (such as Si–OH and –COOH) *via* acid–base treatment. The experimental results indicated that the adsorption capacity and removal rate of RhB were greatly increased by CGFS treated at 298.15 K under neutral conditions. Shi *et al.*[24] converted CGFS into mesoporous composites through K$_2$CO$_3$ alkali melt

School of Urban Planning and Municipal Engineering, Xi'an Polytechnic University, Xi'an 710048, China. E-mail: jingy76@163.com; Tel: +86 29 81369680

activation and exerted the best treatment effect on malachite green at 298 K and pH = 6. The porous carbon-silicon composite prepared by Qiao et al.[25] using CGFS exhibited an adsorption capacity of 208.44 mg g^{-1} for MB. Although great progress has been made, the effect of adsorbents derived from CGFS is still not ideal, and there is still a lot of room for improvement in terms of specific surface area, porosity, adsorption capacity, etc. Therefore, according to the characteristics of CGFS, CGFS-based adsorbents can be prepared to improve adsorption capacity of CGFS, achieve high adsorption effect on dye wastewater, and optimize the resource utilization of CGFS, which is a low-cost, efficient and environmentally friendly treatment method for printing and dyeing wastewater, reflects the sustainable development concept of "treating waste with waste".

In this study, dimethyl diethoxy silane and dodecyl trimethyl ammonium chloride were utilized to modify the surface of CGFS, obtaining dimethyl diethoxy silane-modified CGFS (DDS-CGFS) and dodecyl trimethyl ammonium chloride-modified CGFS (DTAC-CGFS), respectively. Dimethyl diethoxy silane[26] was used to graft hydrophobic methyl groups onto the CGFS surface to enhance hydrophobic interactions with the dye while modulating the surface charge. Conversely, dodecyl trimethyl ammonium chloride,[27] a cationic surfactant, was selected to form a self-assembled layer on CGFS, thereby creating a positively charged interface intended to interact with RhB through a combination of charge-mediated and solvophobic effects. While retaining the metal elements and chemical groups of CGFS, the modifier is grafted onto its surface. The physical and chemical structures of the modified CGFS were analyzed via FTIR, XRD, BET and SEM. Then, adsorption comparison experiments of the RhB, K-GN and H-GL dyes were conducted via DDS-CGFS and DTAC-CGFS. The influence of different pH values and temperatures on the adsorption performance of

RhB, which exerted the best adsorption effect among the dyes, was examined. The adsorption kinetics, isotherms and thermodynamics were analyzed to further explain the adsorption mechanism of RhB dyes. This study aimed to develop an efficient dye adsorbent, provide a theoretical basis, and explore potential approaches to developing low-cost adsorbents from solid waste.

2 Materials and methods

2.1 Materials

Dimethyl diethoxy silane (DDS, 99.5%) was purchased from Nanjing Youpu Chemical Co., Ltd, and dodecyl trimethyl ammonium chloride (DTAC, 98%) was purchased from Sinopharm Group Chemical Reagent Co., Ltd. Coal gasification fine slag was provided by Shaanxi Coal Industry Chemical Group Yulin Chemical Co., Ltd.

2.2 Preparation of adsorbents

Due to the high moisture content of the raw coal gasification slag, it was necessary to dry the raw coal gasification slag before the experiment. The procedure was as follows: the wet slag was rinsed with deionized water, then the filter was pumped several times to wash away the dregs, and finally, the fine coal gasification slag was oven-dried at 373.15 K for 12 h. After being cooled to room temperature, it was sieved through a mesh grinder to obtain the fine coal gasification slag (CGFS).

In a conical flask, 10 mL of DDS was added to 90 mL of ethanol solution, maintaining a water/ethanol ratio of 1 : 100. Then, 10.0 g of CGFS was weighed and added to the mixed solution. In another conical flask, 10 mL of 0.04 mol L^{-1} DTAC solution was mixed with ethanol solution in the same proportion, and 10.0 g of CGFS was added to the flask. The two conical flasks were separately stirred to ensure thorough mixing and
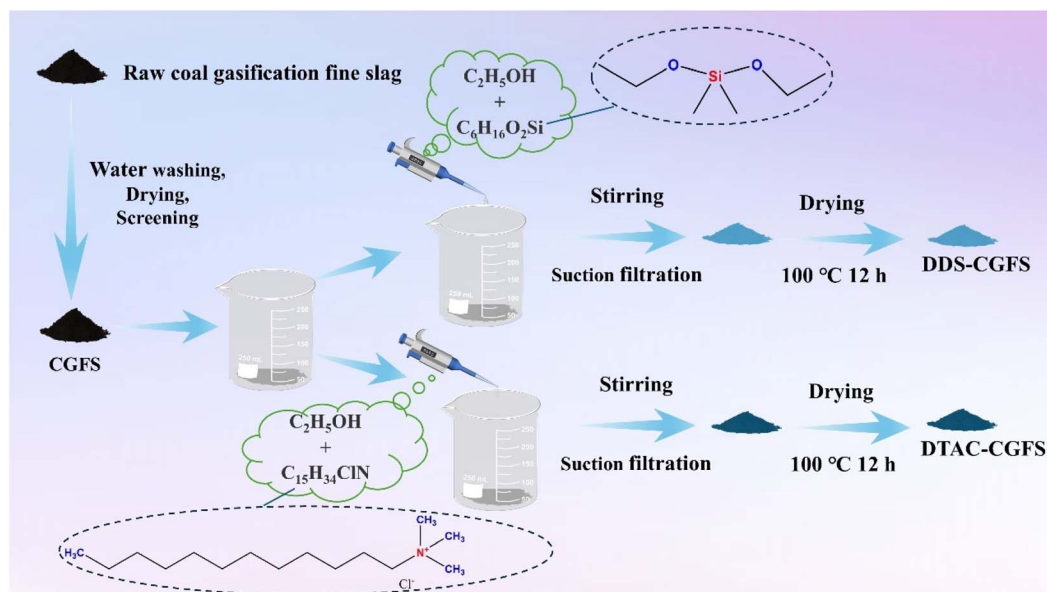

Fig. 1 Flowchart of the preparation of DDS-CGFS and DTAC-CGFS.

reaction between CGFS and the solution. Subsequently, the coal gasification fine slag contained in the conical flask was sucked and filtered and then repeatedly rinsed with deionized water. Finally, the materials were oven-dried at 373.15 K. CGFS modified with DDS is called DDS-CGFS, whereas CGFS modified with DTAC is called DTAC-CGFS. The preparation processes of DDS-CGFS and DTAC-CGFS are presented in Fig. 1.

2.3 Adsorption experiment

This study aimed to investigate the effects of pH value, temperature, and adsorption time on the adsorption properties of dyes, thereby enhancing our understanding of the adsorption behavior of materials for three specific dyes. The experimental procedure is outlined as follows: A 100 mL dye solution with a concentration of 100 mg L^{-1} was added to a 250 mL conical flask, with pH values adjusted in the range of 3 to 11. Then, 0.1 g each of CGFS and modified coal gasification fine slag (DDS-CGFS, DTAC-CGFS) were introduced into the solution. The conical flask was placed in a shaker set at different water bath temperatures (298.15–328.15 K), with a rotation speed fixed at 120 r min^{-1} for a duration of 12 hours. After the reaction period, the dye solution was allowed to stand for some time before being filtered through a filter paper. The absorbance of each dye solution was measured using a UV spectrophotometer at their respective maximum absorption wavelengths. Corresponding concentrations were determined based on absorbance readings referenced against standard curves for each dye solution. The formula used to calculate adsorption capacity is as follows:

$$Q_t = (C_0 - C_t)V/m \qquad (1)$$

where Q_t (mg g^{-1}) denotes the adsorption capacity of the adsorbent at time t; C_0 (mg L^{-1}), the initial concentration of the dye; and C_t (mg L^{-1}), the concentration of the dye at time t.

The mathematical expressions of PFO, PSO and ID are as follows:

$$q_t = q_e \times (1 - e^{-k_1 t}) \qquad (2)$$

$$q_t = k_2 q_e^2 t/(1 + k_2 q_e t) \qquad (3)$$

$$q_t = k_t t^{1/2} + c \qquad (4)$$

where q_e (mg g^{-1}) denotes the equilibrium adsorption capacity; k_1 (L min^{-1}) and k_2 (g mg^{-1} min^{-1}), the adsorption rate constants of PFO and PSO, respectively; k_t, the intra-particle diffusion constant; c, the effect of the boundary layer on the adsorption rate (the higher the value of c, the greater the effect).

The mathematical expressions of the Langmuir, Freundlich and Dubinin–Radushkevich (D–R) models are as follows:

$$q_e = q_m C_e K_L/(1 + K_L C_e) \qquad (5)$$

$$q_e = K_F C_e^{\frac{1}{n}} \qquad (6)$$

$$\ln Q_e = \ln q_m - k\varepsilon^2 \qquad (7)$$

where C_e (mg L^{-1}) denotes the equilibrium concentration; Q_e (mg g^{-1}), the equilibrium adsorption capacity; q_m (mg g^{-1}), the saturated adsorption capacity; K_L (L mg^{-1}), the Langmuir adsorption constant; K_F, the Freundlich equation constant; and $\frac{1}{n}$, the magnitude of the adsorption strength. k, ε is the parameter of the D–R adsorption isotherm. The mathematical expressions of the adsorption thermodynamic models are as follows:

$$K_d = q_e/C_e \qquad (8)$$

$$\ln K_d = \Delta S/R - \Delta H/RT \qquad (9)$$

$$\Delta G = -RT \ln K_d \qquad (10)$$

where K_d denotes the thermodynamic equilibrium constant and R (8.314 J mol^{-1} K^{-1}) is the universal gas constant.

2.4 Characterization

The composition of surface functional groups was analyzed via Fourier transform infrared spectroscopy (FTIR, Nicolet iS50) in the wavelength range of 4000–500 cm^{-1}. The mineral phase composition on the surface of the material was analyzed via X-ray diffraction (XRD, Rigaku D/max2200pc). CuKα was used as
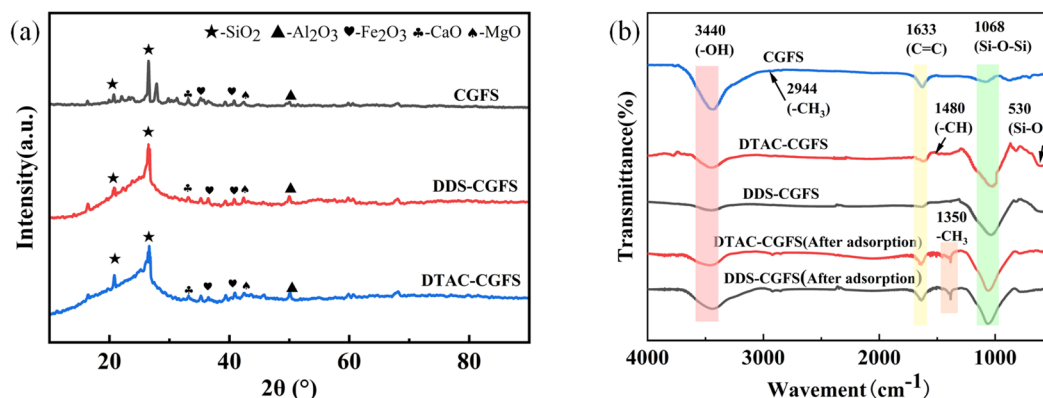

Fig. 2 (a) XRD and (b) FTIR spectra of CGFS, DDS-CGFS and DTAC-CGFS.

the target material. The scanning range was 5–90°, and the scanning speed was 8° min^{-1}. The nitrogen adsorption–desorption isotherm was measured using a physical adsorption analyzer to determine the specific surface area and pore structure of the sample. The BET adsorption–desorption isotherm was used to determine the specific surface area and pore structure of the sample. The surface morphology of the sample at different magnifications was observed using an emission scanning electron microscope (SEM, JSM-6460) to capture detailed microstructure characteristics. The elemental composition and content were analyzed *via* EDS.

3 Results and discussion

3.1 Structural characterization of materials

3.1.1 XRD analysis. Fig. 2(a) presents the comparison of the XRD patterns of CGFS, DDS-CGFS, and DTAC-CGFS. The main inorganic minerals of CGFS are quartz (SiO_2)[28] and a small amount of hematite (Fe_2O_3), cubic magnesite (MgO) and corundum (Al_2O_3). For DTAC-CGFS and DDS-CGFS, the XRD patterns did not significantly change; only the diffraction peak intensity exhibited a slight different. Compared with the XRD patterns of the original fine slag samples, the characteristic peaks remained the same, and no new miscellaneous peaks appeared.

3.1.2 FTIR analysis. Fig. 2(b) shows the FTIR spectra of CGFS, DDS-CGFS, and DTAC-CGFS. After heat treatment at 373.15 K, CGFS produced a wide absorption peak at about 3440 cm^{-1}, which was inferred to be the –OH group, mainly due to the tensile vibration of adsorbed water. The peak was also more susceptible to the influence of absorbed water in the surrounding environment. At about 2944 and 2827 cm^{-1}, there were two weak absorption peaks generated by the vibration of the –CH$_3$ groups. The peak at about 1633 cm^{-1} was generated by the stretching vibration of the C=C group and represented the aromatic structure. The higher the content of the aromatic structure, the better the thermal stability. The peaks at about 1068 cm^{-1} were caused by the asymmetric stretching of Si–O–Si. For DTAC-CGFS, compared with the original slag, new FTIR bands appeared at 530 cm^{-1}, which was derived from the bending vibration of Si–O. The peaks in the range of 1480 and 2900–3450 cm^{-1} corresponded to the stretching vibration of the

–CH and –OH groups, and the intensity of FTIR bands was enhanced, which indicated that the modification was successful and dodecyl trimethyl ammonium chloride cations appeared on the surface of the fine slag. The absorption peaks of DDS-CGFS at 3434 cm^{-1} indicated that the Si–OH produced by hydrolysis of silane coupling agent had a condensation reaction with the Si–OH on the surface of the fine slag, suggesting that the silane agent was grafted on the surface of the fine slag in the form of chemical bond. The peak at 1100 cm^{-1} was caused by the stretching vibration of the Si–O–C bond, whereas the peak in the range of 1035–1080 cm^{-1} indicated the presence of the Si–O–Si bond. All these proved that dimethyl diethoxy silane successfully modified coal gasification fine slag and organic silane was successfully grafted. By comparing before and after adsorption, a new FTIR peak appeared at 1330–1390 cm^{-1}, which could be the characteristic peak of RhB, indicating that RhB was successfully adsorbed.

3.1.3 Pore structure analysis. Fig. 3(a) shows the N$_2$ adsorption–desorption isotherms of CGFS, DDS-CGFS and DTAC-CGFS. The adsorption amount of N$_2$ by DDS-CGFS and DTAC-CGFS rapidly rose in the low relative pressure range and increased with the increase in relative pressure, indicating the existence of a micropore filling effect and a micropore structure inside the material. In the region with high relative pressure ($P/P_0 > 0.4$), type VI hysteresis rings appeared in all materials, indicating a rich mesoporous structure. The hysteresis rings appeared as the capillary condensation enabled the N$_2$ molecules to condense and fill mesoporous channels under normal pressure. The adsorption and desorption isotherms did not overlap as the adsorption and desorption processes started at different liquid levels. The shape of the hysteresis loop is consistent with the classification of the International Union of

Table 1 Pore structure parameters

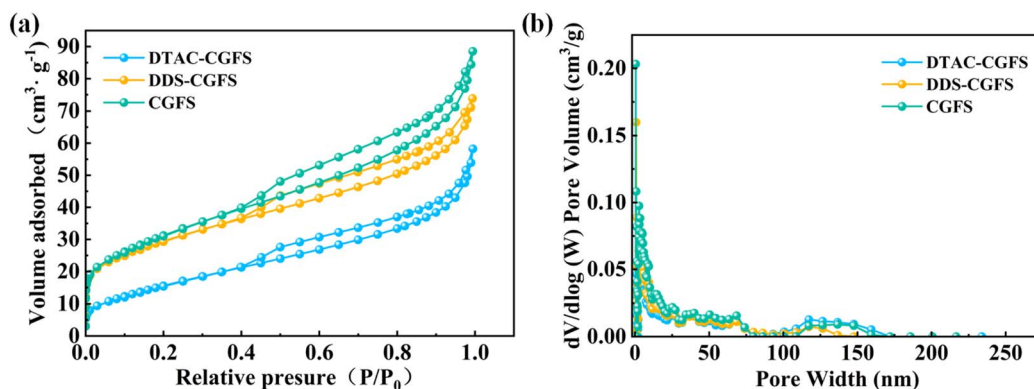| Adsorbents	Specific surface area (m^2 g^{-1})	Average aperture size (nm)	Total pore volume (cm^3 g^{-1})
CGFS	109.19	4.78	0.13
DDS-CGFS	100.58	4.39	0.11
DTAC-CGFS	59.16	5.59	0.08

Fig. 3 (a) N$_2$ adsorption–desorption isotherms and (b) pore-size distribution of CGFS, DDS-CGFS and DTAC-CGFS.

Theoretical and Applied Chemistry (IUPAC), which belongs to the H4-type hysteresis loop, suggesting that the material has a rich mesoporous structure. The pore-size distribution shown in Fig. 3(b) indicates that the pore sizes of CGFS, DDS-CGFS and DTAC-CGFS are mainly distributed in the range of 0–7 nm, and there are abundant mesoporous and microporous structures. As shown in Table 1, the specific surface area of DDS-CGFS is about 2 times that of DTAC-CGFS, which is more conducive to dye adsorption.

3.1.4 Morphological analysis. Fig. 4(a1–c2) presents SEM images of CGFS, DDS-CGFS and DTAC-CGFS. Fig. 4(a1, a2) shows the surface morphology of CGFS. The particle size is uneven, the shape is mainly amorphous, and there are some relatively fine glassy spheroids, which may be SiO_2, with a particle size of about 12–15 μm. Fig. 4(b1, b2) presents the SEM image of DDS-CGFS. After modification, the overall microscopic morphology of DDS-CGFS does not significantly change, but it can be observed that the surface of the material becomes rough, and some finer substances and flocculent substances appear, which exactly indicates the successful preparation of DDS-CGFS. Fig. 4(c1, c2) presents the SEM image of DTAC-CGFS, similar to DDS-CGFS, the overall microscopic morphology slightly changes, but the material surface is smooth.

Table 2 Atomic percentages of CGFS and DDS-CGFS

Element	CGFS	DDS-CGFS
C	42.72	77.16
O	45.78	20.69
Si	6.41	1.33
Fe	0.86	0.05
Al	2.16	0.21
Ca	0.61	0.05
Other	1.46	0.51

Fig. 4(d) shows the EDS element mapping of DDS-CGFS, whereas Table 2 shows the atomic percentages of CGFS and DDS-CGFS. The C, O, Si, Al and Ca elements are uniformly distributed within the carbon framework, and local co-abundance regions of silicon and oxygen can be observed simultaneously. The C/Si of CGFS is 6.66%, whereas that of DDS-CGFS is 58.01%. This indicates that carbon-containing organic groups were successfully implanted on the surface of CGFS.

3.2 Adsorption performance analysis

3.2.1 Effect of dye type on adsorption performance. Fig. 5(a) shows the adsorption effect diagrams of three
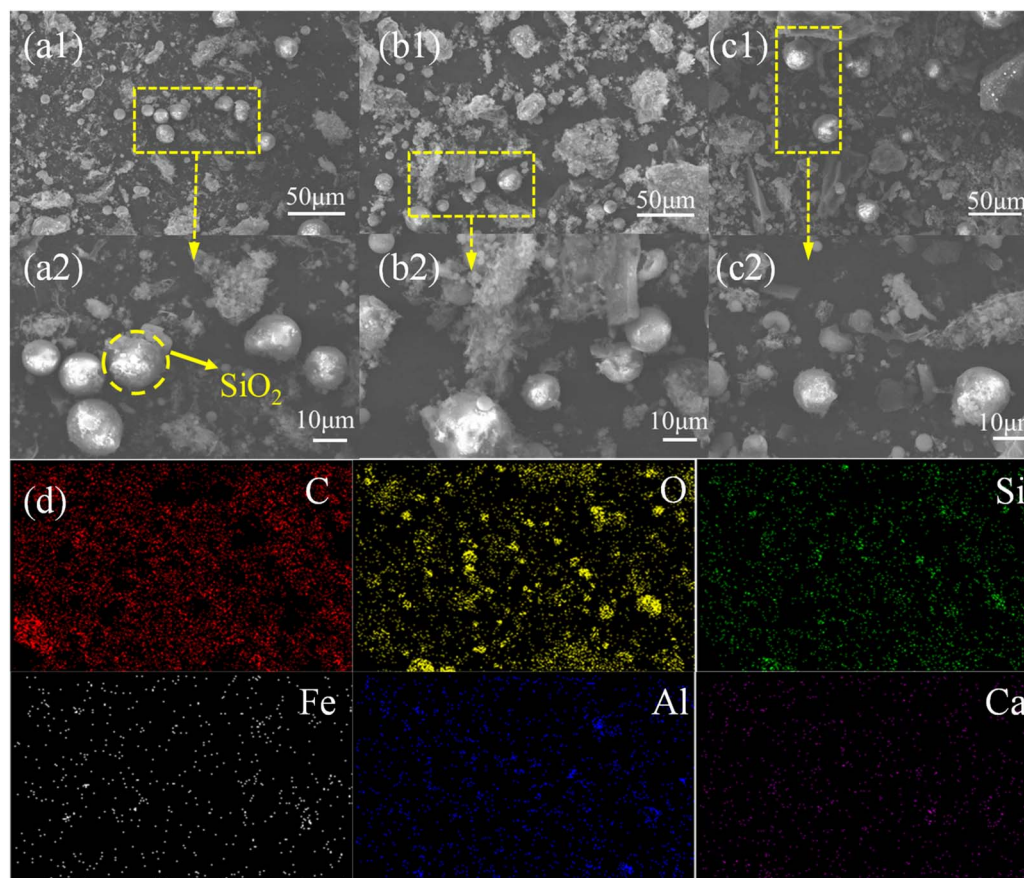

Fig. 4 SEM images of the (a1, a2) CGFS, (b1, b2) DDS-CGFS and (c1, c2) DTAC-CGFS samples at different magnifications. (d) EDS element mapping images of DDS-CGFS.
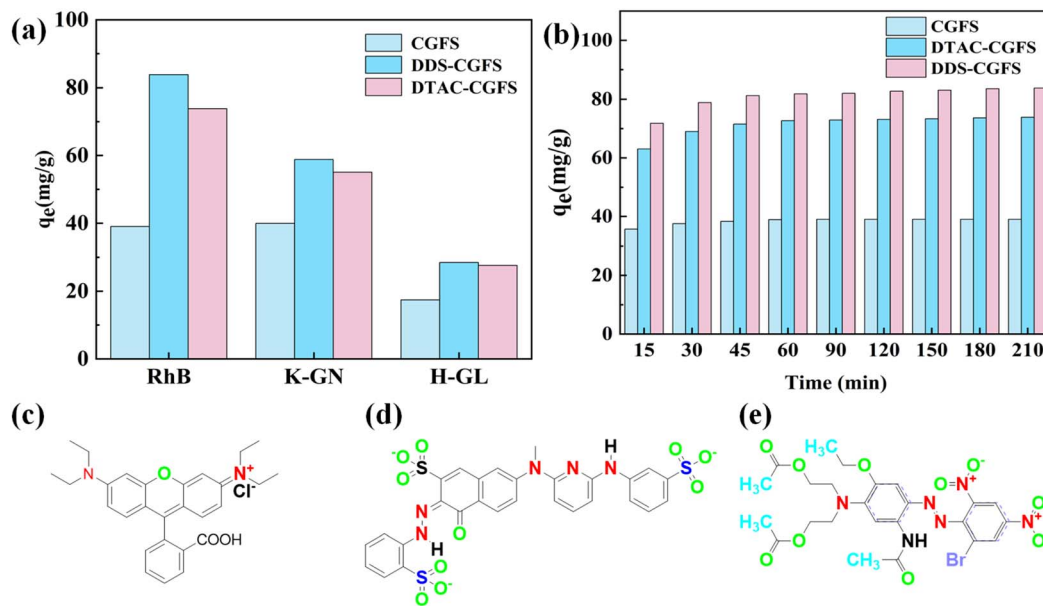
Fig. 5 Effect of (a) dye-type and (b) time on the adsorption performance of adsorbents. Molecular structural formulas of (c) RhB, (d) K-GN, and (e) H-GL.

adsorbents for different dyes, with the solution temperature being 278.15 K and the solution pH value being 7. It can be observed from the figure that the adsorption capacity of the modified coal gasification fine slag for dyes is markedly enhanced. The adsorbents have different adsorption capacities for the three dyes, and all exhibit a selective order of RhB > K-GN > H-GL. This may be because the molecular weight of RhB, enabling it to easily reach the internal active sites through the pore structure of the adsorbent. Fig. 5(c)–(d) show the molecular structures of the three dyes, the molecular weights of the three dyes, from smallest to largest, are all RhB, K-GN, H-GL. Among the three adsorbents, the most effective one was DDS-CGFS, with an adsorption capacity of 83.81 mg g^{-1} for RhB. The second was DTAC-CGFS, which reached an adsorption capacity of 73.84 mg g^{-1}. The adsorption capacities of both adsorbents increased by 114.68% and 89.14%, respectively, compared with CGFS. This experiment shows that the modified adsorbent had the best adsorption effect on RhB. Therefore, subsequent experiments continued to explore the influence of different factors on the adsorption effect of RhB.

It can be found that the specific surface area of DDS-CGFS and DTAC-CGFS both decreased after modification; however, their adsorption capacity for RhB markedly increased. This suggests that the enhancement of performance mainly stems from the alteration of surface chemical properties rather than the optimization of physical structure. First, the surface of DDS-CGFS was grafted with dimethylsiloxane chains. This modification not only enhances affinity with the RhB aromatic ring but also consumes part of the surface hydroxyl groups, optimizes the interface charge, and thereby weakens the electrostatic repulsion with the RhB cation. Synergistic enhancement of the hydrophobic effect and electrostatic attraction was achieved, and an adsorption layer characterized by long alkyl chains and

cation groups was formed on the DTAC-CGFS surface. The long alkyl chain forms a hydrophobic micro-region at the interface, and RhB molecules can effectively localize within this area. Although the cationic group causes the surface to carry a strong positive charge and generate electrostatic repulsion with RhB, the hydrophobic distribution effect is sufficient to overcome this repulsive force and becomes the main driving force for adsorption.

Fig. 5(b) shows the adsorption properties of three materials for RhB under the influence of different time. As shown in the figure, the adsorption capacity of the three dye materials gradually increases over time. The maximum adsorption capacity of CGFS for RhB is 49.94 mg g^{-1}, whereas the minimum is 39.05 mg g^{-1}. For RhB, the adsorption capacity of DDS-CGFS increased from 71.81 to 83.81 mg g^{-1}, whereas that of DTAC-CGFS increased from 63.05 to 73.84 mg g^{-1}, corresponding to increases of 16.71% and 17.11%, respectively.

3.2.2 Effect of pH. In adsorption experiments, pH is an important factor that influences the surface charge of the adsorbent in the solution as well as the ionization and molecular structure of RhB.[29] The adsorption effect of the adsorbent on RhB under the influence of different pH values is presented in Fig. 6(a). In this figure, the adsorption capacity variation trends of the three samples are similar. With the increase in pH, the adsorption capacities of DDS-CGFS, DTAC-CGFS, and CGFS gradually decreased to 97.36, 77.47, and 39.05 mg g^{-1}, respectively, reaching the maximum value at pH = 3. Meanwhile, at pH = 11, they decreased to 17.34%, 22.73% and 35.95%, respectively. At pH = 3, RhB exists in the form of cations and monomer molecules. RhB cations enter the adsorbent through electrostatic attraction and are more easily captured. As the pH value increases, RhB exists in the form of an amphoteric ion,
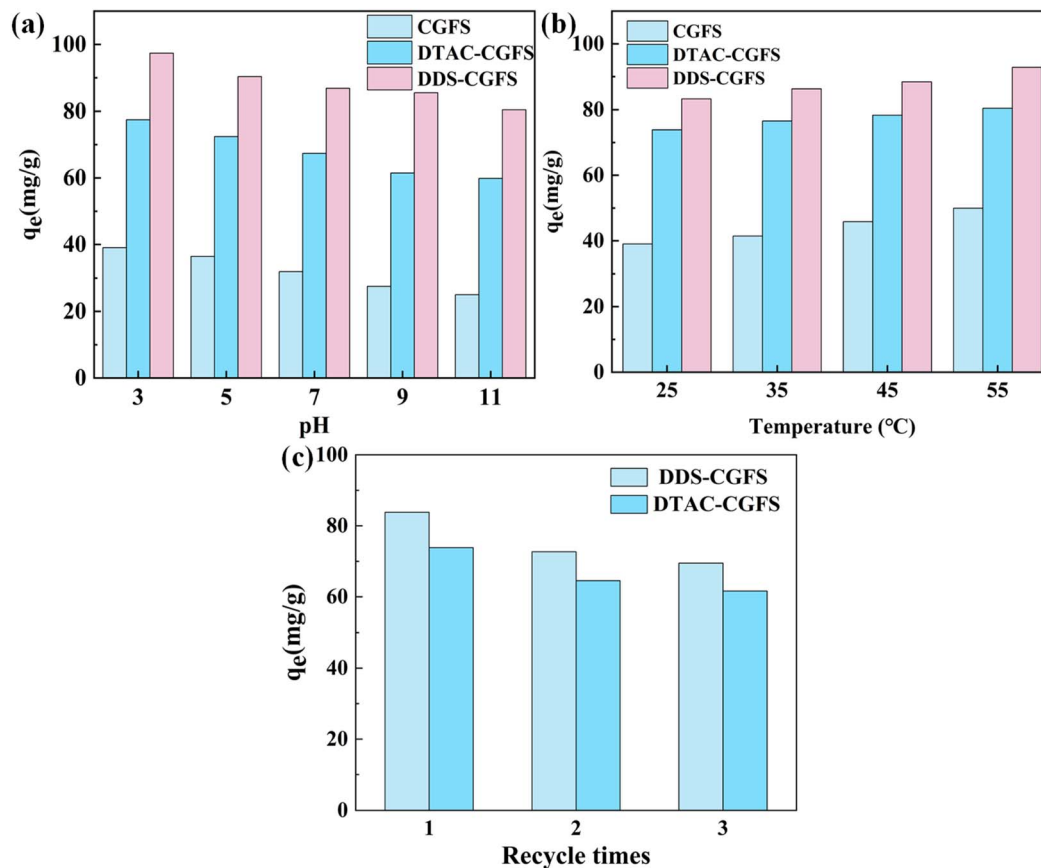
Fig. 6 Effect of (a) pH and (b) temperature on the adsorption capacities of CGFS, DDS-CGFS and DTAC-CGFS. (c) Repeatability experiments of DDS-CGFS and DTAC-CGFS.

hindering its entry into the pore structure of the adsorbent, thereby leading to a decrease in adsorption capacity.

3.2.3 Effect of temperature. Fig. 6(b) shows the adsorption properties of three materials under the influence of different temperatures. As shown in the figure, with the increase in solution temperature, the adsorption capacities of the three materials for the RhB dye also increase, indicating that the adsorption process is an endothermic reaction. CGFS, DDS-CGFS and DTAC-CGFS reached their maximum values at 328.15 K, which were 49.94, 80.45 and 92.82 mg g^{-1}, respectively. Compared with the minimum values, they increased by 27.88%, 8.95% and 11.42%, respectively. This may be because as the temperature rises, the rate of molecular movement gradually increases, and resistance to molecular movement decreases, making it easier for dye molecules to combine with the adsorption sites in the adsorbent, thereby enhancing the adsorption capacity of the adsorbent.

3.2.4 Adsorption recoverability. To verify the cycling stability of DDS-CGFS and DTAC-CGFS, three cycling adsorption tests were conducted on the adsorbents. Under the conditions of 298.15 K and pH = 7, 0.1 g of the adsorbent was dispersed in 100 mL of dye solution (100 mg L^{-1}) for 24 hours. As illustrated in Fig. 6(c), after three cycles, DDS-CGFS and DTAC-CGFS still demonstrated good adsorption capacity for RhB, suggesting

that these two adsorbents have good cycling stability and recyclability.

3.2.5 Adsorption kinetics. To elucidate the key factors affecting adsorption rate and mechanism, pseudo-first-order kinetics (PFO) and pseudo-second-order kinetics (PSO) models as well as intramolecular diffusion (ID) models were used to fit the adsorption processes of CGFS, DDS-CGFS and DTAC-CGFS. Table 3 summarizes the dynamic parameters obtained by fitting. The fitting results of PFO and PSO are presented in Fig. 7(a and b). In the PSO model, the correlation coefficient (R^2) of DDS-CGFS and DTAC-CGFS for the RhB reached 0.99, which was significantly higher than that of the PFO model and was extremely close to 1, whereas the RSME of PSO was lower than that of PFO. The theoretical adsorption capacity of DDS-CGFS for RhB was 84.49 mg g^{-1}, which was very close to the experimental adsorption capacity of 83.81 mg g^{-1}. The results indicated that the adsorption process of DDS-CGFS for the RhB was more consistent with the PSO model. Similarly, the adsorption process of RhB by DTAC-CGFS was consistent with the PSO model. Moreover, the RSME of PSO was lower. This result suggests that the adsorption process may involve electrostatic force, electron transfer and other mechanisms.[30,31] The adsorption process of RhB by CGFS is more consistent with the correlation coefficient of the PSO fitting curve (The R^2 of PSO is large). However, it must be emphasized that the PSO model is

Paper

Table 3 Adsorption kinetic parameters fitted based on the PFO, PSO and ID models

Model	Parameters	CGFS	DDS-CGFS	DTAC-CGFS
PFO	q_e(cal)/(mg g^{-1})	47.79 ± 1.89	80.54 ± 1.13	71.59 ± 0.87
	k_1/(mg min g^{-1})	0.09 ± 0.01	0.22 ± 0.02	0.17 ± 0.01
	R^2	0.5423	0.7741	0.8983
	RMSE	3.55	3.59	2.65
PSO	q_e(cal)/(mg g^{-1})	53.03 ± 2.47	84.49 ± 0.29	75.57 ± 0.28
	k_2/(mg min g^{-1})	0.002 ± 0.0009	0.005 ± 0.0001	0.004 ± 0.001
	R^2	0.7809	0.9916	0.9939
	RMSE	2.46	0.69	0.65
ID	K_{t1}(mg/(g min$^{1/2}$))	2.85 ± 0.75	4.00 ± 0.65	4.46 ± 0.85
	C_1	25.71 ± 4.57	54.62 ± 3.33	42.42 ± 4.33
	R^2	0.8194	0.8626	0.9688
	RMSE	1.5242	3.13	4.06
	K_{t2}(mg/(g min$^{1/2}$))	$0/52 \pm 0.26$	0.32 ± 0.02	0.17 ± 0.01
	C_2	44.63 ± 2.29	79.22 ± 3.29	71.31 ± 0.12
	R^2	0.7965	0.7926	0.9795
	RMSE	0.1878	0.14	0.06

empirical, and its good fit alone cannot serve as conclusive evidence of chemical adsorption. The final determination of the adsorption mechanism requires a comprehensive assessment by combining the isotherm model, thermodynamic parameters and spectroscopic characterization.

Fig. 7(c) shows the linear fitting results of the ID model of CGFS, DDS-CGFS and DTAC-CGFS. The entire adsorption process can be fitted with two straight lines that do not pass through the origin, which suggests that the entire adsorption process is limited not only by surface diffusion but also by intra-particle diffusion.[32] The first straight line represents the diffusion of the dye from the liquid phase to the surface of the material, whereas the second straight line represents the intra-particle diffusion of the dye into the pores of the material.[33] The
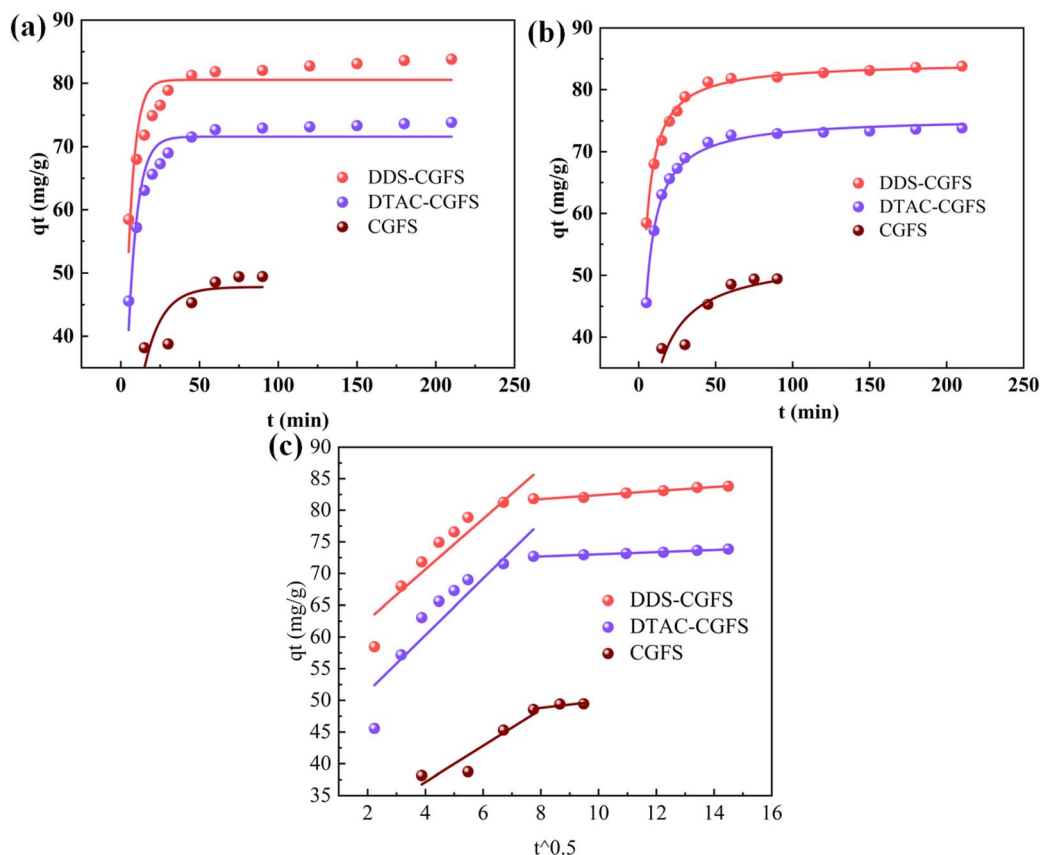

Fig. 7 (a) PFO, (b) PSO, and (c) ID fitting diagram of CGFS, DDS-CGFS and DTAC-CGFS.
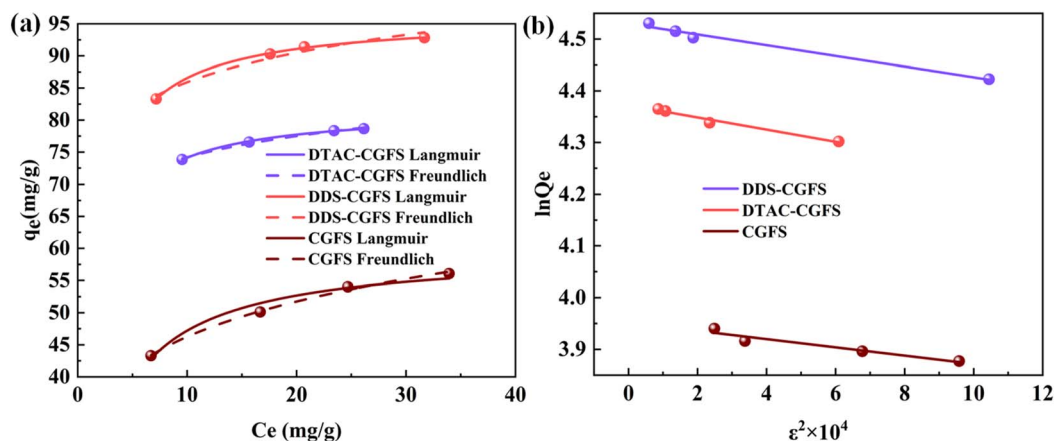
Fig. 8 Adsorption isotherm model of CGFS, DDS-CGFS and DTAC-CGFS: (a) Langmuir and Freundlich and (b) D–R models.

higher slope of the first line indicates a faster diffusion rate on the outer surface; thus, intra-particle diffusion is the main rate-limiting step in the adsorption process. In the ID model, the C_2 value is greater than the C_1 value, indicating that the influence of boundary layer on the adsorption rate is more significant. The good fitting of the pseudo-second-order kinetic model indicates that the adsorption rate may be controlled by the interaction between the active sites on the adsorbent surface and the adsorbate, and this process involves electron sharing or exchange.

3.2.6 Adsorption isotherm. The Langmuir, Freundlich and Dubinin–Radushkevich (D–R) models were used for adsorption isotherm fitting. The fitting curve is presented in Fig. 8 and the parameters in Table 4. According to the data in the table, the

adsorption processes of RhB are more consistent with the Langmuir isotherm model, and the correlation coefficient R^2 is higher. This suggests that the Langmuir model is more suitable for describing the adsorption of DDS-CGFS and DTAC-CGFS on RhB, indicating that the adsorption process is monolayer adsorption, that is, each adsorption site is occupied by only one dye molecule. For CGFS, the R^2 of the Freundlich model is greater than that of the Langmuir model, suggesting that the Freundlich model is more suitable for describing this adsorption behavior and confirming that the adsorption of RhB by CGFS is multilayer adsorption. In the Freundlich model, $1/n$ denotes the favorability of the adsorption; a $1/n$ value greater than 0.5 indicates that the adsorption is easy to perform, whereas a $1/n$ value greater than 2 indicates otherwise. In this experiment, the $1/n$ values were all less than 0.5, indicating that adsorption is easy to perform. Table 3 shows that the average adsorption energy E of all samples is significantly lower than 8 kJ mol^{-1}. E values below 8 kJ mol^{-1} usually indicate that the adsorption process is dominated by physical adsorption,[34] suggesting that adsorption may mainly occur through van der Waals forces or micropore filling. This seems to have a surface contradiction with the good fitting of the PSO model. However, this reflects the complexity of the real adsorption system: the PSO model may describe the rate-limiting steps of surface binding or diffusion, whereas the D–R energy reflects the average intensity of the overall adsorption interaction. The two describe the adsorption process from different dimensions and are not completely mutually exclusive.

3.2.7 Adsorption thermodynamics. We further analyzed adsorption mechanism from the perspective of adsorption

Table 4 Adsorption isotherm parameters of DDS-CGFS and DTAC-CGFS

Model	Parameters	CGFS	DDS-CGFS	DTAC-CGFS
Langmuir	K_L (L mg^{-1})	0.38 ± 0.06	0.91 ± 0.02	0.98 ± 0.03
	q_m/(mg g^{-1})	59.59 ± 1.39	96.08 ± 0.19	81.70 ± 0.15
	R^2	0.9572	0.9991	0.9986
	RMSE	1.64	0.23	0.14
Freundlich	K_F	31.87 ± 0.69	72.29 ± 2.14	64.19 ± 0.74
	$1/n$	0.16 ± 0.007	0.07 ± 0.01	0.06 ± 0.003
	R^2	0.9946	0.9657	0.9882
	RMSE	0.58	1.35	0.34
D–R	E (KJ mol^{-1})	3.95 ± 0.01	4.53 ± 0.05	4.37 ± 0.05
	R^2	0.8951	0.9771	0.9684
	RMSE	0.01	0.01	0.01

Table 5 Thermodynamic parameters for the adsorption of dyes by DDS-CGFS and DTAC-CGFS

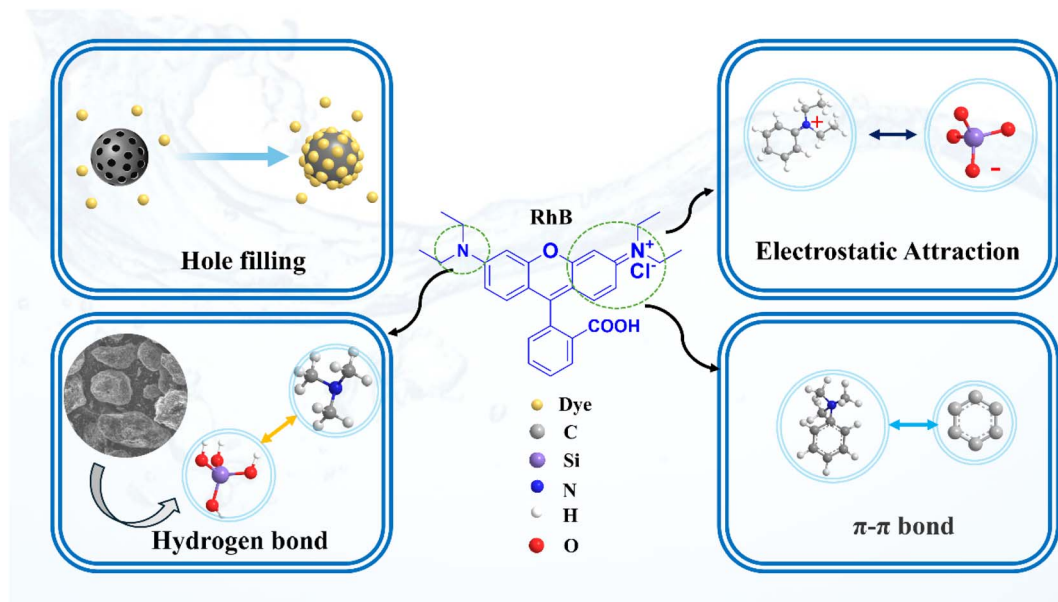|	ΔG (KJ mol^{-1})					
Adsorbents	298.15 K	308.15 K	318.15 K	328.15 K	ΔH (KJ mol^{-1})	ΔS (KJ mol^{-1})
CGFS	−8.979	−10.252	−11.525	−12.798	6.0912	0.0541
DDS-CGFS	−3.98	−4.71	−5.37	−6.98	24.63	0.09
DTAC-CGFS	−2.57	−3.03	−3.40	−3.86	10.02	0.04

Fig. 9 Adsorption mechanism diagram.

thermodynamics. The thermodynamic parameters include ΔH (enthalpy change), ΔG (Gibbs free energy) and ΔS (entropy change); the specific values are shown in Table 5. The table shows values ranging from 298.15 to 328.15 K. ΔG decreases with the increase in temperature, and the negative values of ΔG for RhB by DDS-CGFS and DTAC-CGFS indicate that the adsorbents are highly adsorbent and the adsorption is spontaneous.[35] The ΔG value is between -20 and 0 KJ mol^{-1}, indicating that the adsorption process is physical adsorption.[36] When multiple forces (e.g., electrostatic attraction and hydrogen bonding) coexist, the adsorption process may conform to the proposed secondary kinetics; however, the thermodynamic parameter ΔG may fall within the range of physical adsorption. This apparent contradiction is due to the synergy of multiple weak interactions. Therefore, the adsorption of dye by the two adsorbents is considered to be a synergistic effect of physisorption and chemisorption. The ΔH and ΔS values are positive, indicating that the adsorption process absorbs heat and the interface disorder between the solution and the adsorbent increases. With the increase in temperature, the adsorption process is more favorable, suggesting that the modified coal gasification fine slag can adsorb dye better at

a high temperature. The absolute value of the adsorption enthalpy change ΔH is less than 40 kJ mol^{-1}, indicating that the adsorption force is mainly a physical action. Combined with the analysis of D–R energy E, although the PSO model fits well, thermodynamic and isotherm evidence is more supportive of the physical–chemical mixed adsorption mechanism.

3.2.8 Adsorption mechanism. After a systematic study of the influencing factors of adsorption, combined with the results of adsorption kinetics, isothermal models, thermodynamic analysis and characterization, we believe that the adsorption process of dyes by modified CGFS involves the joint contribution of physical and weak chemical effects. Taking the adsorption of RhB by DDS-CGFS as an example, its adsorption mechanism can be reasonably explained as follows: physical adsorption is mainly reflected in the processes of molecular diffusion and pore filling, which is supported by the intraparticle diffusion model. DDS-CGFS has a large specific surface area and rich multi-level pore structure (mainly micropores and mesopores), which is conducive to the progress of molecular diffusion and pore filling, and may exert a capillary effect, thereby promoting RhB adsorption. FTIR analysis revealed that there are oxygen-containing functional groups

Table 6 RhB adsorption capacity of different adsorbents

Absorbent	q_{max} (mg g^{-1})	References
DDS-CGFS	92.82	This work
DTAC-CGFS	80.45	This work
Based on graphene oxide and molecular sieves (GO/4A-3 material)	62.81	37
Molecular sieves prepared using CGFS (ZMS-5 material)	23.00	38
Hydrothermal conversion of bamboo shoot shells into biochar (BHC-800 material)	85.80	39
Activated carbon treated with NH$_4$Cl and NaOH (ZBAC-3 material)	1375.8	40
Pyridine-based covalent organic framework (TAPP-DBTA-COF material)	1254	41
Metal–organic skeleton (MIL-68(Al) material)	227	42

(such as –OH) and siloxane structures (Si–O$^-$) on the material surface. RhB exhibits cationic characteristics under experimental conditions; thus, there may be hydrogen bond interactions and electrostatic attraction between the dye cations and negatively charged sites. Meanwhile, both the adsorbent and dye molecules contain aromatic structures, and the contribution of π–π stacking interactions cannot be ruled out. It should be noted that the above mechanism explanations are based on existing characterizations and model analyses. Among them, the pore structure parameters and diffusion models provide relatively direct evidence for physical adsorption, whereas the electrostatic and hydrogen bond interactions are mainly based on reasonable inferences of surface chemistry and dye properties. π–π stacking, on the other hand, is a reasonable speculation that awaits further direct verification. Overall, the adsorption process is extremely likely the result of the synergistic action of multiple mechanisms. These mechanisms may coexist and promote each other, jointly enhancing the adsorption effect of DDS-CGFS on RhB. Fig. 9 presents a schematic diagram of these potential interactions.

To better evaluate the adsorption performance of the two synthetic materials, Table 6 presents a comparison of their adsorption capacity for RhB. Compared with adsorbents exhibiting high adsorption capacity, such as ZBAC-3, the synthesis methods of the two adsorbents synthesized in this study are simpler, and the materials used are waste pollutants. Comprehensively taking into account the adsorption capacity and cost performance of the adsorbents, the application prospects of the two materials synthesized in this study are better.

4 Conclusions

In this study, DDS-CGFS and DTAC-CGFS were successfully prepared *via* surface modification of CGFS. These two materials exhibit high adsorption capacity for RhB, particularly DDS-CGFS. This is mainly attributed to the unique synergistic effect of physical adsorption and chemisorption. Analysis of structural properties revealed that the modified CGFS induces no significant change in phase structure. In terms of chemical structure, the Si–OH and Si–O–C FTIR bands are found in the FTIR spectra of DDS-CGFS, and the –CH$_2$ and –CH groups appear in the FTIR spectra of DTAC-CGFS. BET analysis revealed that the specific surface area of DDS-CGFS was 100.58 m^2 g^{-1} and that of DTAC-CGFS was 59.16 m^2 g^{-1}. DDS-CGFS possessed a higher specific surface area, favoring dye adsorption. The adsorption kinetics and thermodynamics showed that the adsorption of dyes by DDS-CGFS and DTAC-CGFS was mainly physical and chemical, which may involve electrostatic force and other mechanisms. The adsorption process is endothermic and spontaneous. The adsorption of dyes by the two materials mainly depends on the interaction of the hydrogen and π–π bonds. In addition, physical adsorption exerted a significant effect. This study provides theoretical basis and practical value for the resource utilization of CGFS and the treatment of dye wastewater. Future studies should continue to focus on the resource utilization of CGFS and its practical application in the treatment of dye wastewater.

Author contributions

Changwei Bai: material preparation, data collection and analysis, writing – original draft. Jing Yang: writing – review & editing, funding acquisition, conceptualization, methodology.

Conflicts of interest

There are no conflicts to declare.

Data availability

The authors declare that the data supporting the findings of this study are available within the paper. Should any raw data files be needed in another format, they are available from the corresponding author upon reasonable request. Source data are provided with this paper.

Acknowledgements

References

1 D. H. Liu, W. D. Wang, Y. N. Tu, G. L. Ren, S. L. Yan, H. Y. Liu and H. He, *J. Clean. Prod.*, 2022, **363**, 132426.

2 X. B. Sun, M. Chu, X. Shi, J. F. Dong and Y. Y. Liu, *Sep. Purif. Technol.*, 2025, **360**, 130964.

3 Y. Xu, T. Zheng, G. B. Guo, J. H. Li, H. J. Luo, H. S. Jiang, W. D. Ai, Y. Li and C. D. Wei, *Polymer*, 2025, **322**, 128160.

4 L. G. V. Buonfiglio, I. A. Mudunkotuwa, M. H. A. Alaiwa, O. G. V. Calderón, J. A. Borcherding, A. K. Gerke, J. Zabner, V. H. Grassian and A. P. Comellas, *Environ. Health Perspect.*, 2017, **125**(7), 077003.

5 Y. X. Guo, W. Y. Hu, G. R. Feng, Y. H. Zhao, C. Q. Li, X. X. Wang and J. H. Ma, *Powder Technol.*, 2024, **435**, 119460.

6 C. Y. Yu, J. J. He, M. X. Tan, Y. X. Hou, H. Zeng, C. B. Liu, H. M. Meng, Y. J. Su, L. J. Qiao, T. Lookman and Y. Bai, *Adv. Funct. Mater.*, 2022, **32**(52), 2209365.

7 J. J. Zhang, X. L. Yan, X. Y. Hu, R. Feng and M. Zhou, *Chem. Eng. J.*, 2018, **347**, 640–647.

8 J. J. Zhang, W. Liu, F. He, M. Song, X. Huang, T. Shen, J. W. Li, C. Zhang, J. Zhang and D. L. Wang, *Chem. Eng. J.*, 2022, **438**, 135619.

9 J. Yang, X. D. Yang, D. B. Jia and G. J. Zou, *J. Xi'an Polytech. Univ.*, 2021, **35**(2), 1–8.

10 M. T. Moustafa, *Sci. Rep.*, 2023, **13**, 4493.

11 N. V. Heise, D. Major, S. Hoenke, M. Kozubek, I. Serbian and R. Csuk, *Molecules*, 2022, **27**(7), 2220.

12 Z. Chai, B. Liu, P. Lv, Y. H. Bai, J. F. Wang, X. D. Song, W. G. Su and G. S. Yu, *Fuel*, 2023, **333**, 126318.

13 W. Ma, X. Yang, L. G. Lin, H. Li, H. Y. Shang, H. Wu, M. F. Hou, Z. N. Guo, Z. T. Liu, J. Yang and B. W. Li, *J. Membr. Sci.*, 2025, **723**, 123937.

14 Z. P. Sun, L. Gan, Y. S. Liu, Q. P. Liu, Q. Gao and Y. Ni, *Desalination*, 2025, **600**, 118464.

15 Y. J. Shen, Q. H. Xu, R. R. Wei, J. L. Ma and Y. Wang, *Ultrason. Sonochem.*, 2017, **38**, 681–692.

16 Y. B. Zhou, J. Lu, Y. Zhou and Y. D. Liu, *Environ. Pollut.*, 2019, **252**(Part A), 352–365.

17 Y. Dehmani, D. S. P. Franco, J. Georgin, R. Mghaiouini, B. B. Mohammed, R. acimi, T. Lamhasni, E. C. Lima, N. E. Messaoudi and A. Sadik, *Environ. Surf. Interfaces*, 2025, **3**, 103–111.

18 D. Vamvuka, K. Stergiou, E. Sdoukou and A. Stratakis, *J. Environ. Chem. Eng.*, 2024, **12**(1), 111907.

19 Y. C. Mei, S. T. Zhuang and J. L. Wang, *Sci. Total Environ.*, 2025, **968**, 178898.

20 M. Najafi, S. Abednatanzi, P. G. Derakhshandeh, F. Mollarasouli, S. Bahrani, E. S. Behbahani, P. V. D. Voort and M. Ghaedi, *Coord. Chem. Rev.*, 2022, **454**, 214332.

21 S. Rojas and P. Horcajada, *Chem. Rev.*, 2020, **120**(16), 8378–8415.

22 T. Skorjanc, D. Shetty and A. Trabolsi, *Chem*, 2021, 7, 882–918.

23 Y. B. Huang, F. X. Bao, J. W. Wang, Z. L. Gu, H. T. Zhang, J. Y. Wang, J. M. Dan, Y. B. Liao, C. L. Hong and J. C. Liu, *Sep. Purif. Technol.*, 2025, **353**, 128397.

24 X. Z. Shi, L. H. Xu, J. Tian, K. Q. Shu, Z. J. Wang, K. Xue, H. Q. Wu, D. HuiWang and G. HuanLi, *J. Water Proc. Eng.*, 2025, **69**, 106670.

25 Q. X. Qiao, B. Tang, X. Y. Men, F. Q. Gu, K. M. Dong, Z. J. Sun, J. J. Wang, L. W. Kong and Y. H. Bai, *J. Clean. Prod.*, 2024, **435**, 140498.

26 Q. Q. Su, W. Q. Liu, W. R. Wang and Y. F. Liu, *Green Build.*, 2008, (05), 23–25.

27 H. Zhang, M. J. Cai and Q. F. Wu, *Mod. Chem. Ind.*, 2012, **32**(12), 61–66.

28 Q. Y. Wang, Y. H. Bai, P. Lv, X. D. Song, M. Ma, Y. Shen, G. S. Yu and M. Yao, *Fuel*, 2023, **339**, 127437.

29 L. Aljerf, *J. Environ. Manage.*, 2018, **225**, 120–132.

30 H. Dolas, *J. King Saud Univ. Sci.*, 2023, **35**(3), 102559.

31 M. Y. Nassar, E. A. Abdelrahman, A. A. Aly and T. Y. Mohamed, *J. Mol. Liq.*, 2017, **248**, 302–313.

32 Y. C. Dong, S. B. Mao, F. Q. Guo, R. Shu, J. M. Bai, L. Qian and Y. H. Bai, *Energy*, 2022, **238**, 121867.

33 M. Wang, R. Z. Xie, Y. Chen, X. Q. Pu, W. J. Jiang and L. Yao, *Bioresour. Technol.*, 2018, **268**, 726–732.

34 L. T. Wang, J. Yang, J. C. Xia, L. Yang, Q. Zhang and Z. E. Li, *Basic Sci. J. Text. Univ.*, 2023, **36**(01), 26–35.

35 A. Oussalah, A. Boukerroui, A. Aichour and B. Djellouli, *Int. J. Biol. Macromol.*, 2019, **124**, 854–862.

36 S. S. Fan, J. Tang, Y. Wang, H. Li, H. Zhang, J. Tang, Z. Wang and X. D. Li, *J. Mol. Liq.*, 2016, **220**, 432–441.

37 X. Liu, Y. Q. Guo, C. RanZhang, X. L. Huang, K. Ma and Y. F. Zhang, *Sep. Purif. Technol.*, 2022, **286**, 120400.

38 N. Yuan, K. Q. Tan, X. L. Zhang, A. J. Zhao and R. Guo, *Chemosphere*, 2022, **303**, 134839.

39 Y. R. Hou, G. G. Huang, J. H. Li, Q. P. Yang, S. R. Huang and J. JunCai, *J. Anal. Appl. Pyrolysis*, 2019, **143**, 104694.

40 B. Y. T. Shan Xue, H. Li Zu, X. Yu Ma, Y. Xu, M. H. Li, C. X. Fang and H. Sheng Tao, *Colloids Surf., A*, 2021, **618**, 126489.

41 K. J. Chang, H. J. Huang, Y. D. Meng, Z. D. Ju, H. Y. Song, L. Zhang, X. Q. Niua and Z. J. Li, *RSC Adv.*, 2023, **13**(34), 23682–23689.

42 M. S. Tehrani and R. Z. Dorabei, *RSC Adv.*, 2016, **6**(33), 27416–27425.